Korean J. Chem. Eng., 38(5), 1032-1042 (2021)
DOI: 10.1007/s11814-021-0762-z

pISSN: 0256-1115
eISSN: 1975-7220

Fabrication of hydrophobic ZIFs based composite membrane with high CO_2 absorption performance

Li Xu, Yu Qin, Liying Liu, Juntian Xiao, and Zhongwei Ding†

Beijing Key Laboratory of Membrane Science and Technology, College of Chemical Engineering, Beijing University of Chemical Technology, Beijing 100029

(*Received 15 November 2020 • Revised 4 February 2021 • Accepted 8 February 2021*)

Abstract−The membrane contactor has been considered an effective device to capture CO_2, but its performance is limited by membrane wetting phenomena. In this work, the ZIF-8/ZIF-L (zeolitic imidazolate framework) based composite membrane with excellent hydrophobic stability and CO_2 permeability was successfully fabricated by coating the dense layer on the porous PVDF (polyvinylidene fluoride) substrate. The dense layer was developed by evenly incorporating ZIF-8 nanocrystals and ZIF-L nanosheets into the polydimethylsiloxane (PDMS) polymer. The as-prepared membrane possessed competitive hydrophobicity with a water contact angle (WCA) of 131.8°. And after a ten-day immersion test in CO_2 absorbent, the WCA only declined by 9.8%, exhibiting excellent hydrophobic stability. Besides, the CO_2 permeability of the composite membrane was 61.8×10^{-8}·mol·m^{-2}·s^{-1}·Pa^{-1} with an ideal CO_2/N_2 separation factor of ~20, which was effectively improved in comparison with the control membrane. In the CO_2 absorption experiment, the prepared membrane achieved the competitive CO_2 flux of 3.02×10^{-3}·mol·m^{-2}·s^{-1} when the liquid velocity was 0.25 m·s^{-1} and displayed robust long-term operating stability. Finally, the AC impedance technique was applied to continuously monitor the wetting state of composite membranes, which further investigated their anti-wetting ability.

Keywords: Hydrophobic Composite Membrane, Zeolitic Imidazolate Frameworks (ZIFs), CO_2 Absorption, Membrane Wetting, Membrane Contactor

INTRODUCTION

The gas-liquid membrane contactor (GLMC) has been recognized as a promising device to absorb carbon dioxide (CO_2), which is closely associated with global warming [1]. In 1985, Qi and Cussler first applied this membrane module to capture CO_2 [2]. Since then, many researchers have been working on this area [3-6]. When CO_2 is absorbed in GLMC, the absorbent and gas flow on both sides of the membrane respectively, which helps to enhance the CO_2 absorption performance [7]. The membrane used in GLMC will inevitably increase the resistance of CO_2 mass transfer. More severely, once the membrane pores are intruded by the absorbent solution, the mass transfer resistance will rise sharply [8]. Thus, the alleviation of the membrane wetting phenomenon is vital for the commercial application of GLMC.

Commercial polymer membranes, such as polytetrafluoroethylene (PTFE), polyvinylidene fluoride (PVDF), and polypropylene (PP) are widely used in the CO_2 absorption process [9]. Among which PTFE possesses the best hydrophobicity, but the CO_2 absorption performance in long-term operation seems not very competitive [10]. Let alone PVDF and PP membranes, whose membrane pores are easily wetted by CO_2 absorbents, such as the diethanolamine (DEA) aqueous solution [11]. Hence, the alleviation of membrane wetting is the key to improving CO_2 absorption performance. A composite membrane composed of a dense hydrophobic layer and the porous substrate has the potential to solve this issue and then enhance CO_2 absorption performance [12]. For example, Dai et al. found that under certain operating conditions, the long-term CO_2 absorption flux of the Teflon-PP composite membrane was better than that of the porous PTFE membrane [13].

However, compared with porous supports, the composite membrane with a dense layer will inevitably increase the CO_2 mass transfer resistance. To compensate for this disadvantage, the dense layer should be highly permeable to CO_2. More importantly, if the dense layer fails to maintain its hydrophobicity and is gradually wetted by CO_2 absorbent in a short period, just as the porous support does, the composite membrane loses its advantage. And under this situation, the composite membrane will cause bigger CO_2 mass transfer resistance than the wetted porous substrate [14]. Consequently, the dense layer should be much more hydrophobic than the porous substrate, which is the key to alleviating wetting. All in all, the dense layer should be both highly permeable to CO_2 and effectively resistant to CO_2 absorbent within a certain period.

Incorporating nanoparticles into the dense layer is a useful way to deal with the stated obstacles. The incorporated particles can both increase surface hydrophobicity and improve CO_2 permeance of the composite membrane. To elaborate, the filling particle is advantageous to constructing the micro-nano structures, which is the key to fabricating hydrophobic surfaces [15]. Besides, incorporated particles can also provide abundant microcavities, which benefits the permeance of CO_2 gas. Rosli et al. successfully constructed a composite membrane by incorporating modified silica nanoparticles

†To whom correspondence should be addressed.
E-mail: dingzw@mail.buct.edu.cn

into PVDF support and then increased the CO_2 absorption flux from 0.066 $mmol \cdot m^{-2} \cdot s^{-1}$ to 0.232 $mmol \cdot m^{-2} \cdot s^{-1}$ [16].

As one of the commonest ZIFs, ZIF-8 is chemically stable and possesses the appropriate porosity; and due to its good compatibility with polymers, such as PDMS, they are suitable to serve as filler particles in the preparation of composite membranes [17,18]. Therefore, ZIF-8 nanoparticles were used as the main filler particles in this work.

However, the incorporation of filler particles will inevitably result in agglomeration phenomena. Xu et al. found that when the loading ratio of aminosilane-modified ZIF-8 nanocrystals exceeded 5 wt%, agglomeration occurred in the composite membrane surface, which led to the decrease of CO_2 absorption flux [19]. Even using well-designed spraying equipment, when the loading of ZIF-8 nanoparticles reached 40 wt%, serious agglomeration occurred [20]. And it seems inappropriate to decrease the loading ratio to alleviate agglomeration. This is disadvantageous to constructing micro-nano structures and will reduce the mass transfer microcavity provided by ZIF-8 nanoparticles [15,16]. In addition, serious agglomeration will lead to uneven dispersion of filler particles and influence force distribution of the dense layer, which results in surface cracks and tears. These defects seem much more destructive than agglomeration. For example, only several nanoscale cracks could seriously damage the membrane selectivity [21]; therefore, it is important to synthesize a defect-free composite membrane.

ZIF-L, a leaf-shaped two-dimensional ZIFs, was first introduced by Chen et al. [22]. And with the development of composite membrane, ZIF-L nanosheets have been filled into a polymer matrix to improve membrane performance. By incorporating ZIF-L nanosheets, Mao et al. fabricated a high-performance membrane with excellent mechanical strength [23]. Li et al. regulated the molecular sieving effect of the dense layer through in-situ synthesizing two-dimensional ZIF-L within the poly (vinylamine) matrix [24]. In the present work, other than ZIF-8 nanocrystals, ZIF-L nanosheets, of micron scale, were innovatively incorporated to reduce surface defects of the composite membrane and alleviate agglomeration.

The anti-wetting ability is a critical property of composite membranes and worth carefully exploring. AC impedance, an electrochemical measurement technique, has been applied to study membrane properties and the wetting processes. Through this technique, Bannwarth et al. realized the characterization of PP hollow fiber membranes [25]. Xiao et al. used the same technique to monitor the wetting process of both the PVDF flat sheet membrane and the hollow fiber membrane in real-time [26]. In this work, this technique was first introduced to continuously monitor the wetting state of the composite membrane. So, its wetting-resistant ability could be analyzed more thoroughly.

In this study, the ZIFs based composite membrane was successfully constructed and then meticulously characterized. The influence of filler particles on the membrane structure and characteristics was thoroughly investigated. The prepared membranes successively carried out the immersion test, CO_2/N_2 permeance test, CO_2 absorption experiment, and AC impedance test. Through these experiments, the hydrophobic stability, CO_2/N_2 permeability and selectivity, CO_2 absorption performance, and anti-wetting ability were carefully evaluated.

MATERIALS AND METHODS

1. Materials

Porous PVDF substrate was purchased from Beijing Zhongxiyuanda Technology. PDMS (polydimethylsiloxane, 40 cst) was bought from Macklin; MTES (Triethoxymethylsilane, ≥98%), DBTDL (Ditin butyl dilaurate, ≥95%), zinc nitrate hexahydrate ($Zn(NO_3)_2 \cdot 6H_2O$, 99.99%), and 2-methyl imidazole (Hmim, 99%) were provided by Aladdin. Methanol (MeOH, AR) and n-hexane (AR) were used as the solvent. DEA (diethanolamine, ≥98%) and DIW (deionized water, self-made) were mixed to prepare CO_2 absorbent.

2. Preparation of ZIF-8 Nanocrystals and ZIF-L Nanosheets

1.467 g $Zn(NO_3)_2 \cdot 6H_2O$ and 3.245 g Hmim were, respectively, dissolved in 100 ml MeOH to form a homogenous solution; the former solution was rapidly added into the latter under stirring; the ZIF-8 nanocrystals were obtained by centrifugation (washed by fresh MeOH for three times) and dried at 70 °C for 5 h after reaction for 1 h [27].

For the preparation of ZIF-L, a solution of $Zn(NO_3)_2 \cdot 6H_2O$ (0.59 g) in 40 ml DIW was added into the solution of Hmim (1.30 g) in 40 ml DIW with stirring. After reaction under sufficient stirring for 4 h, the product was also obtained by centrifuging (washed by DIW for three times) and dried at 100 °C for 5 h [22].

3. Synthesis of ZIF-8-PDMS-PVDF Composite Membranes

A 10 wt% PDMS solution was prepared by dissolving some PDMS into n-hexane; certain amounts of MTES and DBTDL (the weight ratio of PDMS/MTES/DBTDL is 10 : 3 : 1) were then added under stirring. After adding ZIF-8 nanocrystals (ZIF-8/PDMS ranged from 0 to 40 wt%), the mixture was under ultrasonic dispersion for 20 min to be homogeneous and was then magnetically stirred at ~20 °C for 1 h. The as-prepared mixture was evenly cast on the porous PVDF substrate through a scraper. After the complete evaporation of the n-hexane solvent under vacuum condition at 50 °C for 3 h, the composite membrane was then cured at 110 °C for 6 h to obtain the ZIF-8-PDMS-PVDF composite membrane.

4. Synthesis of ZIF-8-ZIF-L-PDMS-PVDF Composite Membranes

The steps to fabricate ZIF-8-ZIF-L-PDMS-PVDF composite membrane were almost the same as the mentioned procedures. But in this section, ZIF-L nanosheets were also incorporated to repair the surface defects of ZIF-8-PDMS-PVDF membranes. The synthesis diagram is presented in Fig. 1.

5. Characterization

The morphology of ZIF-8 nanoparticles, ZIF-L nanosheets, and the prepared membranes was observed through scanning electron microscopy (SEM, Hitachi, S4800). Energy dispersive X-ray (EDX) was applied to observe the element distribution on the membrane surface. X-ray diffractometer (XRD, Ultima IV, Rigaku) and Fourier transform infrared spectroscopy (FT-IR, Nicolet 8700) were used to analyze the crystal form and chemical functional groups, respectively. The WCA of composite membranes was tested by contact angle meter (SL150E, KINO). The surface roughness of the synthesized membrane was investigated through atomic force microscopy (AFM, Dimension ICON, Bruker). All of the data were averaged over three measurements to ensure accuracy.

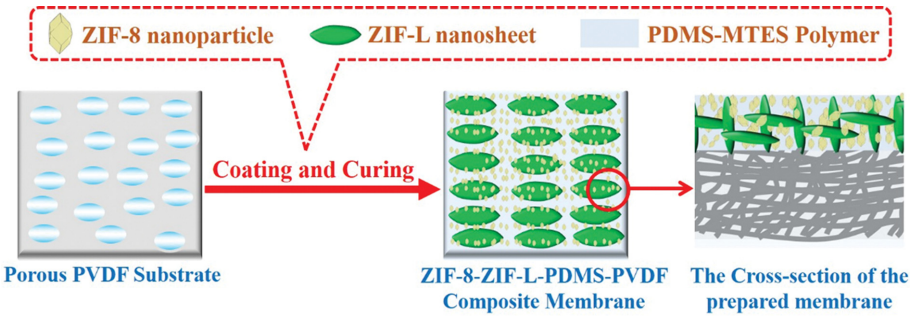

Fig. 1. Schematic diagram of synthesis of the ZIF-8-ZIF-L-PDMS-PVDF composite membrane.

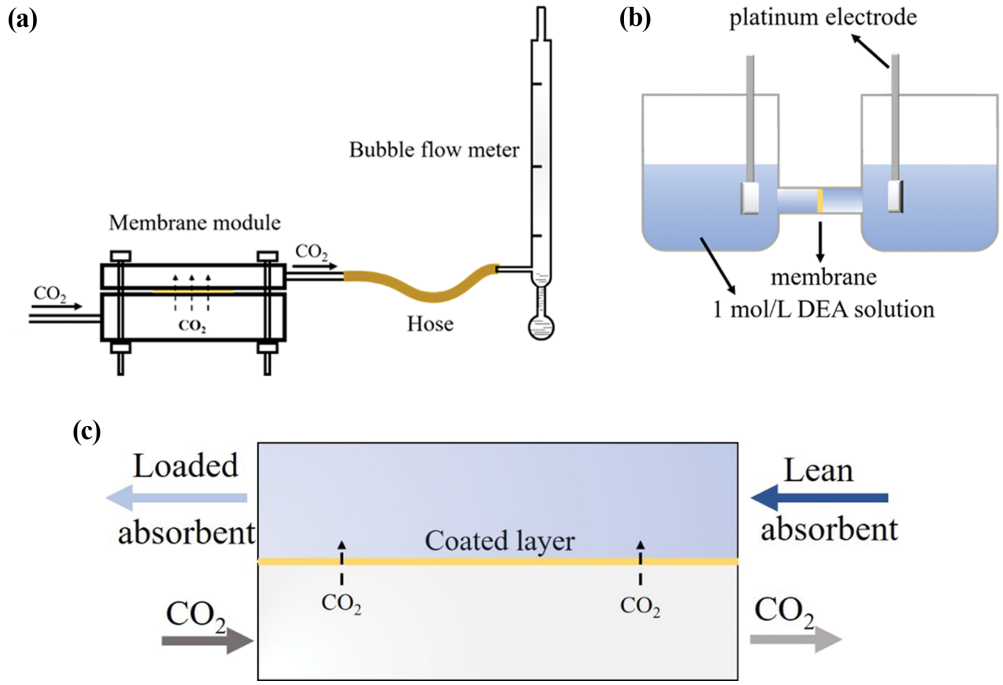

Fig. 2. The Experimental device of (a) gas permeability, (b) AC impedance, (c) CO_2 absorption.

6. Hydrophobic Stability in CO_2 Absorbent

Composite membranes were first immersed in 1 mol/L DEA solution for some time (from 1 day to 10 days) and thoroughly dried in an oven. And then, the WCA of composite membranes was tested. The smaller the reduction of WCA, the higher the hydrophobic stability of the membranes.

7. Gas Permeability Test

The experimental device is shown in Fig. 2(a), taking CO_2 for example. The composite membrane with an effective area (S) of 15.9 cm^2 was fixed in the middle of the test device. The transmembrane pressure Δp was maintained at 10^5 Pa. The bubble flow meter was applied to measure gas permeance of the composite membrane at ~20 °C. The amount of gas i (n_i) was calculated through the ideal gas equation of state. The permeance of gas i (P_i, mol·m^{-2}·s^{-1}·Pa^{-1}) can be obtained through Eq. (1):

$$P_i = \frac{n_i}{St\Delta p} \quad (1)$$

where t (s) is the experiment time.

The ideal separation factor $\alpha_{i,j}$ is defined as Eq. (2):

$$\alpha_{i,j} = \frac{P_i}{P_j} \quad (2)$$

where the P_i and P_j are the gas permeability of i and j, separately.

8. CO_2 Absorption Performance in GLMC

The main part of the flat sheet membrane contactor is shown in Fig. 2(c). The composite membrane was tightly fixed in the middle of the membrane module with CO_2 gas and 1 mol/L DEA solution countercurrently flowing across the raw side and modified side, respectively. To simplify experiment procedures and reduce test errors, the CO_2 absorbent was continuously recycled in each experiment. The effective mass transfer area was 0.0126 m^2. The CO_2 gas velocity was maintained at 1,000 ml·min^{-1}; and the liquid velocity was adjusted from 0.05 m·s^{-1} to 0.25 m·s^{-1} by a peristaltic pump. After the stabilization of the absorption process for 0.5 h, a 100 ml CO_2-loaded absorbent was taken to measure the CO_2 concentration by acid hydrolysis. This experiment was conducted at ~20 °C. Consequently, the CO_2 absorption flux J (mol·m^{-2}·s^{-1}) could be deter-

mined by Eq. (3):

$$J = \frac{CV}{St} \quad (3)$$

where C ($mol \cdot m^{-3}$) is the CO_2 concentration of loaded absorbent; V (m^3) is the total volume of loaded absorbent; S (m^2) represents the mass transfer area; t (s) is the stable operation time.

The long-run CO_2 absorption performance was investigated intermittently. After each round of CO_2 absorption experiment, the composite membrane was still immersed by the DEA solution, which was close to the industrial applications.

9. Monitoring the Membrane Wetting Process

AC impedance was introduced to monitor the membrane wetting process. The test device was inspired by Huang et al. [28], as displayed in Fig. 2(b). To illustrate, the sample membrane was placed at the junction of the H-type electrolytic cell. 1 mol/L DEA aqueous solution was used as both the test solution and electrolyte. The two platinum electrodes were symmetrically and in parallel placed at both sides of the membrane. The assembled electrolytic cell was connected to the electrochemical workstation (CHI600E, Shanghai Chenhua) and computer.

First, the Bode diagram was obtained under specific test parameters (the frequency ranged from 0.1 to 10^5 Hz; the amplitude was fixed at 0.7 V). A particular frequency was then selected from the platform stage of the obtained Bode diagram to ensure that the phase shift was stably close to 0°. After that, the impedance data collected from continuous impedance test could indicate membrane resistance. Finally, the continuous impedance test was conducted at the chosen frequency and the same amplitude (0.7 V) for ~12 h.

RESULTS AND DISCUSSIONS

1. Characterization of ZIF-8 Nanocrystals and ZIF-L Nanosheets

As illustrated in Fig. 3(a), the crystal structure of ZIF-8 nanocrystals and ZIF-L nanosheets was observed via XRD. The distinctive peaks in the XRD pattern of both ZIF-8 and ZIF-L agree well with the previous works [22,27], indicating the successful synthesis of filler particles. The peaks of ZIF-8 crystals are in good accordance with that of the simulated ZIF-8, further confirming its crystallinity. Compared with ZIF-8 nanocrystals, the peak intensity of ZIF-L nanosheet changes considerably, which results from the differences in crystal structure between ZIF-L and ZIF-8; the former is a two-dimensional layered structure, while the latter is a three-dimensional rhombic dodecahedron [29].

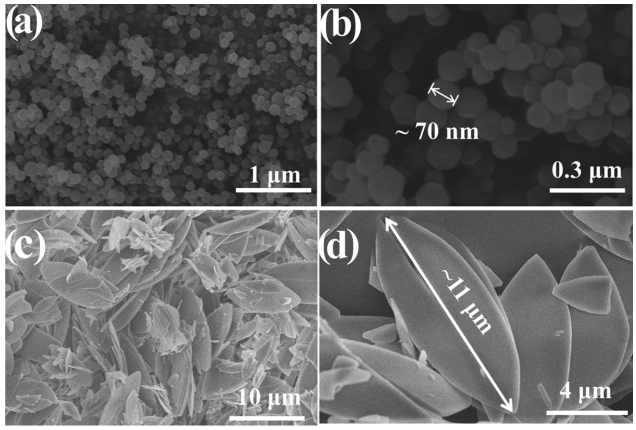

Fig. 4. SEM images of ZIF-8 nanocrystals (a), (b) and ZIF-L nanosheets (c), (d).

The characteristic groups of ZIF-8 nanocrystals and ZIF-L nanosheets were characterized through FT-IR. As presented in Fig. 3(b), the FT-IR spectroscopy of ZIF-8 is almost the same as that of ZIF-L nanosheets since they have the same metal source and organic ligand [30]. Other than Zn-N stretching vibration, recognized at ~420 cm^{-1}, most of the characteristic absorption peaks can be assigned to the vibration of Hmim units. Among these, the intense bands at ~995 and ~1,146 cm^{-1} are associated with C-N stretching; also, the peak at approximately 1,584 cm^{-1} is assigned to C=N stretching. These results conform well with the published researches, further implying the successful preparation of ZIF-8 nanocrystals and ZIF-L nanosheets [19,31].

As shown in Fig. 4, the morphological characteristics of ZIF-8 and ZIF-L were investigated by SEM. The synthesized ZIF-8 nanocrystals with a typical rhombic dodecahedron structure are evenly dispersed (see in Fig. 4(a)), which corresponds to the previous study [27]. Besides, a uniform size of about 65±10 nm (Fig. 4(b)) makes

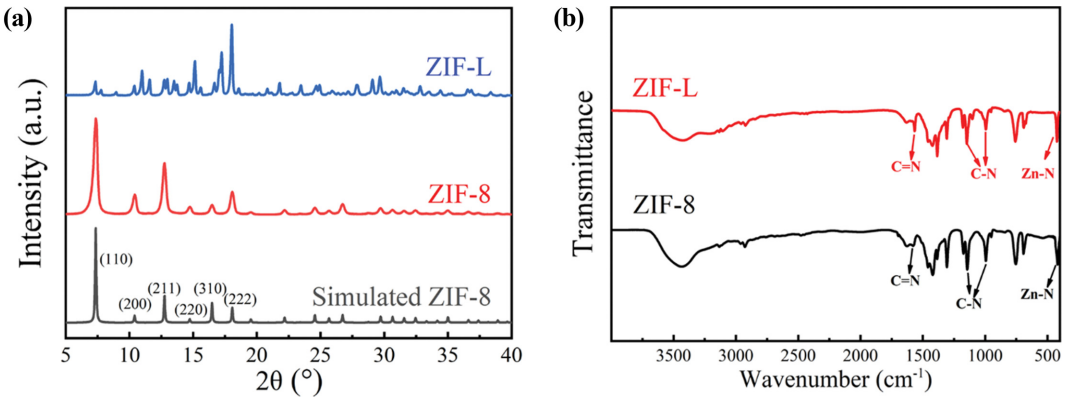

Fig. 3. XRD pattern (a) and FT-IR spectra (b) of ZIF-8 nanocrystals and ZIF-L nanosheets.

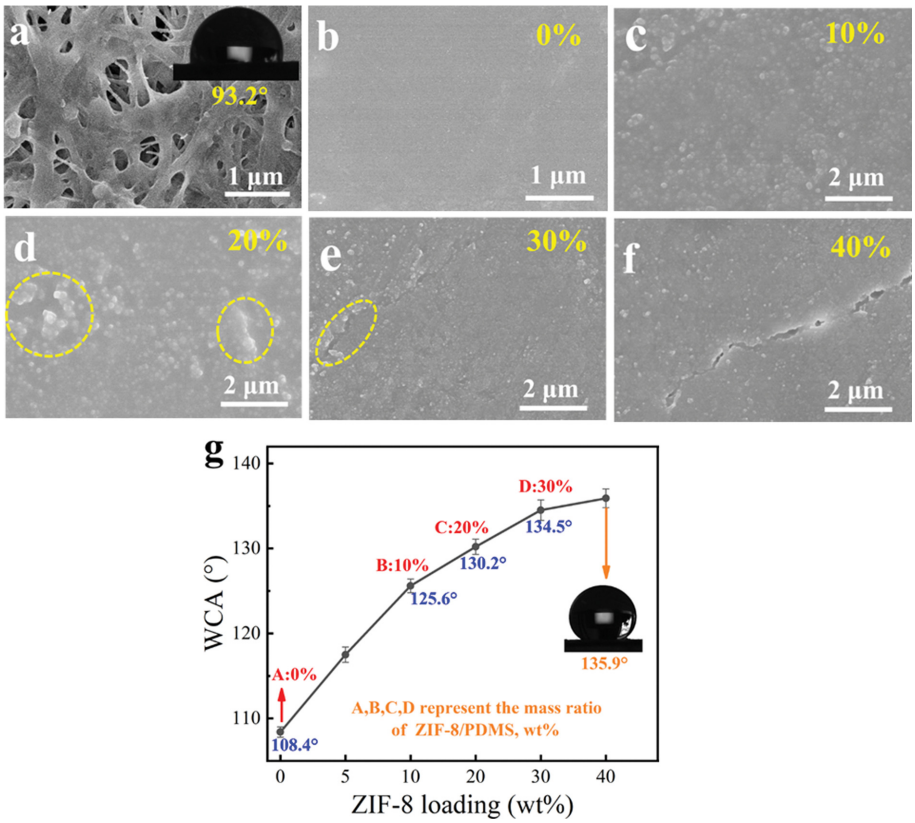

Fig. 5. SEM images (a)-(f) and WCA (g) of ZIF-8-PDMS-PVDF composite membranes.

ZIF-8 nanocrystals appropriate to serve as filler particles. The flat leaf-like two-dimensional structure of prepared ZIF-L nanosheets (Fig. 4(c)) complies well with the literature [22]. With a characteristic size of around 10±1 μm (Fig. 4(d)), ZIF-L nanosheets have the very potential to be used as the skeleton of the composite membrane; this is favorable to enhancing the mechanical strength of the composite membrane.

2. Characterization of ZIF-8-PDMS-PVDF Composite Membranes

The morphology of the PVDF substrate and ZIF-8-PDMS-PVDF composite membrane (the loading ratio ranged from 0 to 40%) was investigated through SEM images. As exhibited in Fig. 5(a), the closely interlinked PVDF fibers are strong enough to serve as the substrate. More importantly, compared with the molecular dynamic diameter of CO_2 (0.33 nm), the pore size is large enough and will not hinder the permeance of CO_2. Unfortunately, this pore structure also results in poor hydrophobicity with a WCA of only 93.2° (inset in Fig. 5(a)). The surface of the ZIF-8 (0%)-PDMS-PVDF composite membrane, referred to as PM, is flat, smooth, and defect-free (Fig. 5(b)). And although the WCA has been increased to 108.4°, this outcome is undesirable (A in Fig. 5(g)). Meanwhile, this coating layer is detrimental to gas permeance. Some ZIF-8 nanoparticles were then loaded to enhance membrane properties. The ZIF-8 filler particles were evenly dispersed when the loading ratio was 10% (Fig. 5(c)). But once this number reached to 20%, as indicated in Fig. 5(d), unwanted agglomeration happened. More seriously, a tiny crack is observed in Fig. 5(e) when this figure is further increased to 30%. And it is destructive that an obvious crack almost stretched across the synthesized composite membrane (see in Fig. 5(f)) at the loading ratio of 40%. Therefore, these surface defects need to be repaired in the following part. Also, as illustrated in Fig. 5(g), the hydrophobicity of the synthesized composite membrane has been improved considerably with the adding of ZIF-8 nanoparticles, which is in good accordance with the reported study [20]. When the loading equals 30%, the WCA increases to 134.5°. And with the increment of ZIF-8 loading to 40%, the WCA is further improved to 135.9°. The improvement of hydrophobicity can be ascribed to the increasing surface roughness of the composite membrane [32].

Fig. 6 displays the surface roughness of the prepared ZIF-8-PDMS-PVDF composite membrane. The average roughness (R_a) is obtained from a test area of 5 μm×5 μm. The R_a of the synthesized membrane increases with the addition of ZIF-8 nanocrystals. When the loading ranges from 10% to 40%, the R_a rises from 55.7 nm to 145 nm, accordingly. These results are in good accordance with the SEM images and the WCA data.

3. Characterization of ZIF-8-ZIF-L-PDMS-PVDF Composite Membrane

In this part, ZIF-L nanosheets were applied to diminish cracks and improve the agglomeration phenomenon and then to construct the defect-free membrane with competitive hydrophobicity. The total mass ratio of ZIFs/PDMS was maintained at 40%. The value of ZIF-L/PDMS gradually increased from 0% to 20%. Meanwhile, the loading ratio of ZIF-8/PDMS was reduced from 40% to

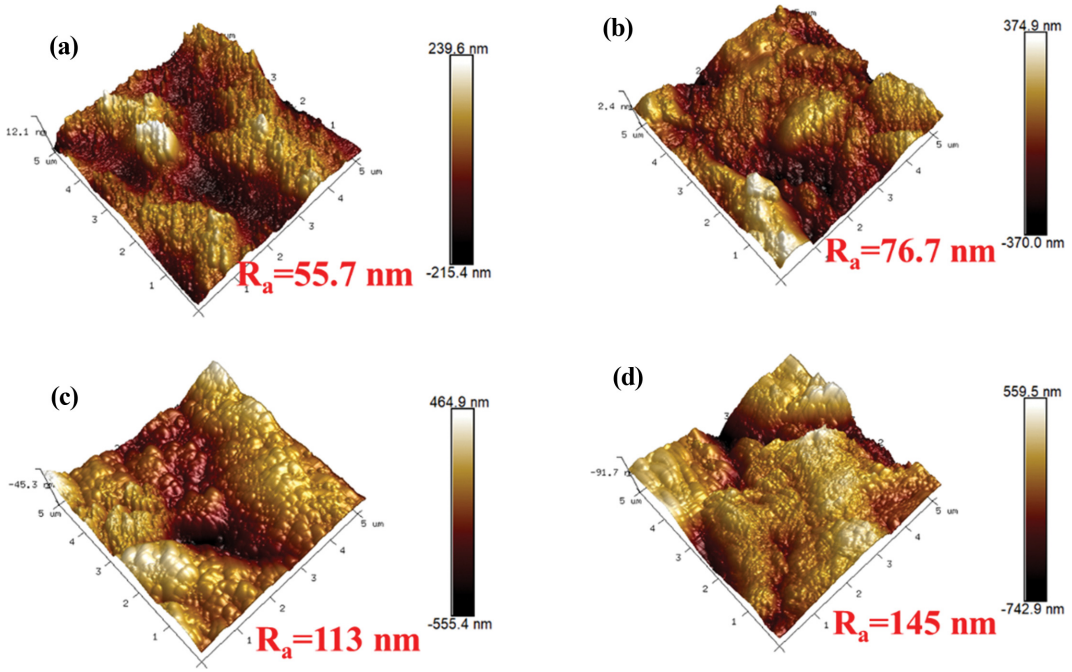

Fig. 6. AFM images of the ZIF-8-PDMS-PVDF composite membrane with the ZIF-8 loading of (a) 10%, (b) 20%, (c) 30%, (d) 40%.

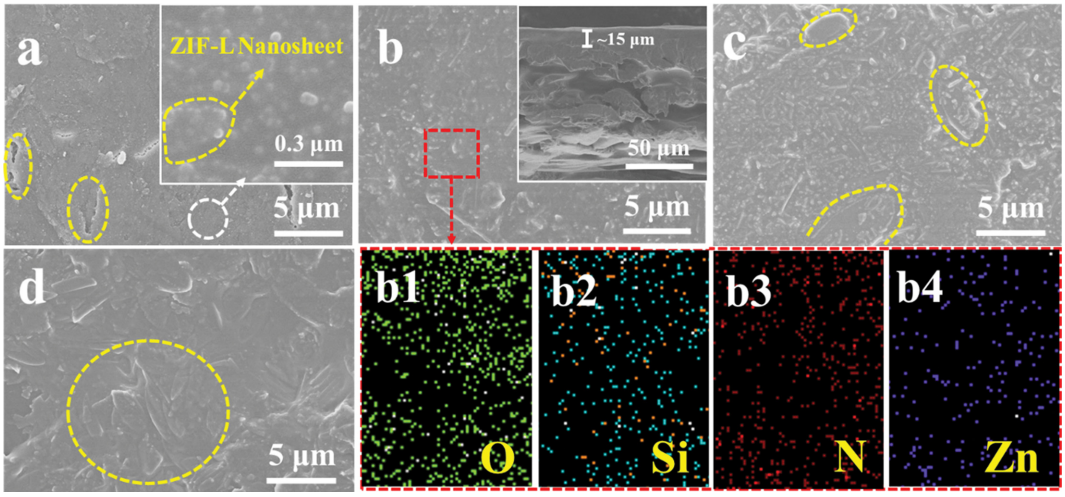

Fig. 7. SEM morphologies of (a) M1, (b) M2, (c) M3, (d) M4, and EDX mappings of (b1) O, (b2) Si, (b3) N, (b4) Zn.

20% step by step. Through this process, the role of which ZIF-L played in the synthesis of the composite membrane was explored. The newly developed ZIF-8(A)-ZIF-L(B)-PDMS-PVDF composite membranes were then symbolically named. The composite membranes used in this part are referred to as M1 (A=35%, B=5%), M2 (A=30%, B=10%), M3 (A=25%, B=15%), M4 (A=20%, B=20%), respectively.

3-1. The SEM Analysis

The morphological features of M1, M2, M3, M4 are presented in Fig. 7. Though there are no destructive cracks when 5% ZIF-L nanosheets are incorporated, M1 still has some tiny cracks (Fig. 7(a)), indicating that the addition of ZIF-L is effective but the amount may be insufficient. And as illustrated in the inset of Fig. 7(a), the outline of the ZIF-L nanosheet can be observed under higher magnification. With the rise of ZIF-L loading ratio to 10%, a defect-free surface was successfully constructed, further indicating the effectiveness of ZIF-L nanosheets in repairing the cracks. And the ZIF-L fragments are scattered across the surface of M2 (see Fig. 7(b)). The inset of Fig. 7(b) exhibits the cross-sectional image of M2. Dense coating with a thickness of ~15 μm is evenly coated on the porous PVDF substrate, and polymer casting solution partly penetrates the substrate, which is advantageous to improving the adhesion between the dense coating and the substrate [33]. The EDX images of M2 are presented in Fig. 7(b) (b1-b4). Elements O and Si indicate the existence of PDMS-METS polymer. The uniform dispersion of element N and Zn implies that the ZIF-8 nanoparticles and ZIF-L nanosheets are uniformly incorporated into the dense layer. When the ZIF-L load ratio reaches 15%, M3 is successfully

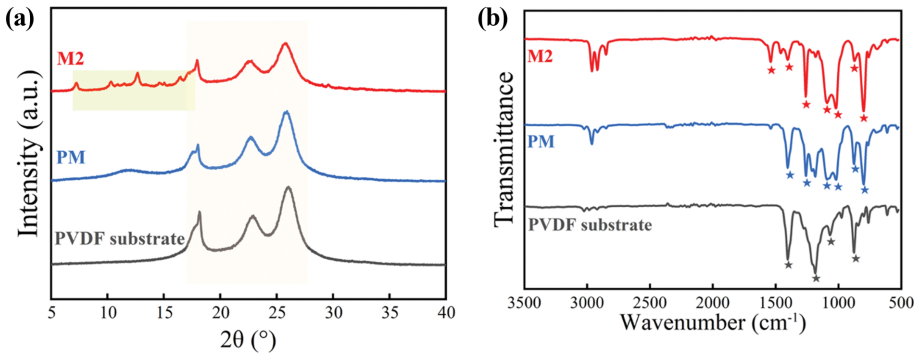

Fig. 8. XRD pattern (a) and FT-IR spectra (b) of PVDF substrate, PM, and M2.

fabricated; many ZIF-L fragments and some whole ZIF-L nanosheets can be observed in Fig. 7(c). As displayed in Fig. 7(d), the slight agglomeration of ZIF-L nanosheets in the surface of M4 implies that there is no need to increase the loading ratio once again.

The leaf-shaped two-dimensional ZIF-L nanosheets with the appropriate size are the key to fabricating defect-free ZIF-8-ZIF-L-PDMS-PVDF composite membranes. The incorporated ZIF-L nanosheets serve as the skeleton of the dense layer, as illustrated in Fig. 1. These skeletons help to improve the force distribution of the dense layer, which diminishes surface cracks, as shown in Fig. 7.

3-2. XRD Analysis

Fig. 8(a) shows the XRD pattern of PVDF substrate, PM, and M2. The characteristic peaks of PVDF roughly range from 16° to 27°, which agrees well with the previous report [34]. Once the PDMS-MTES polymer is coated on the PVDF substrate, these peaks become depressed and smoother, implying desirable compatibility between the porous substrate and the hydrophobic polymer. Furthermore, the distinctive peaks (from ~2.5° to ~18°) of ZIF-8 nanocrystals and ZIF-L nanosheets can be seen in from the XRD pattern of M2, implying the successful incorporation of ZIFs particles into the dense layer.

3-3. FT-IR Analysis

Fig. 8(b) displays the FT-IR spectra of PVDF substrate, PM, and M2, respectively. In comparison with PVDF substrate, the typical peaks of the PM are associated with the stretch of Si-C (~1,260 cm^{-1}, and 865-755 cm^{-1}) and Si-O-Si (1,085-995 cm^{-1}) [35]. After the incorporation of ZIFs, some characteristic peaks emerge. The distinctive bands (~1,095 and 1,146 cm^{-1}) are related to C-N stretching mode, and the absorption peak (~1,584 cm^{-1}) is ascribed to C=N stretch [31]. Therefore, the FT-IR spectra of M2 further indicate the compatibility between filler particles and PDMS-MTES polymer.

3-4. The WCA Test

The WCA data is displayed in Fig. 9, manifesting that the hydrophobicity of the ZIF-8-ZIF-L-PDMS-PVDF composite membrane progressively decreases with the addition of ZIF-L nanosheets. And when the load ratio increases from 0 to 20%, the WCA decreases from 135.9° to 117.3°, indicating the reduction of hydrophobicity.

3-5. Surface Roughness

AFM images were used to explore the mechanism of the mentioned phenomenon. As shown in Fig. 10, AFM images match well

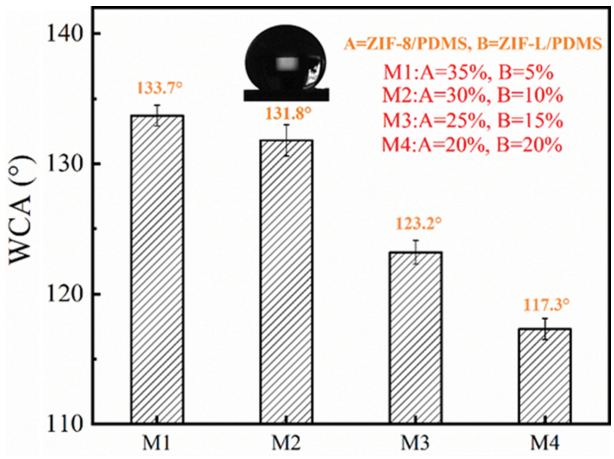

Fig. 9. WCA of the ZIF-8 (A)-ZIF-L (B)-PDMS-PVDF composite membrane.

with the SEM morphology, and the R_a of M1, M2, M3, M4 are, respectively, 99.2 nm, 89.4 nm, 75.8 nm, 66 nm, demonstrating a clear decreasing trend. Consequently, the decrease of hydrophobicity can be ascribed to the reduction in surface roughness. The falling R_a of the synthesized membrane mainly results from the leaf-like two-dimensional structure of ZIF-L nanosheet, which makes the surface smoother [36].

4. Hydrophobic Stability Test

Due to the severe surface defects, M1 was excluded from subsequent tests. Consequently, only M2, M3, M4, and PM were chosen to go through the hydrophobic stability test, among which PM was the control group. As shown in Fig. 11(a), with the increase of immersion time in 1 mol/L DEA solution, the WCA of the membrane sample decreases gradually. The WCA of PM reduces to 70.6°, with a decline of ~35% in this experiment. The WCA reduction of M2, M3, M4 in this test is, respectively, 9.8%, 15.2%, 23%, which is much better than that of the PM, indicating that the incorporation of filler particles can effectively improve the hydrophobic stability of the composite membrane. Also, this excellent hydrophobic stability is the precondition of the long-term CO_2 absorption experiment.

5. Gas Permeability Test

The CO_2 and N_2 permeance of PM, M2, M3, M4 are separately displayed in Fig. 11(b). Both CO_2 and N_2 permeance of PM are rela-

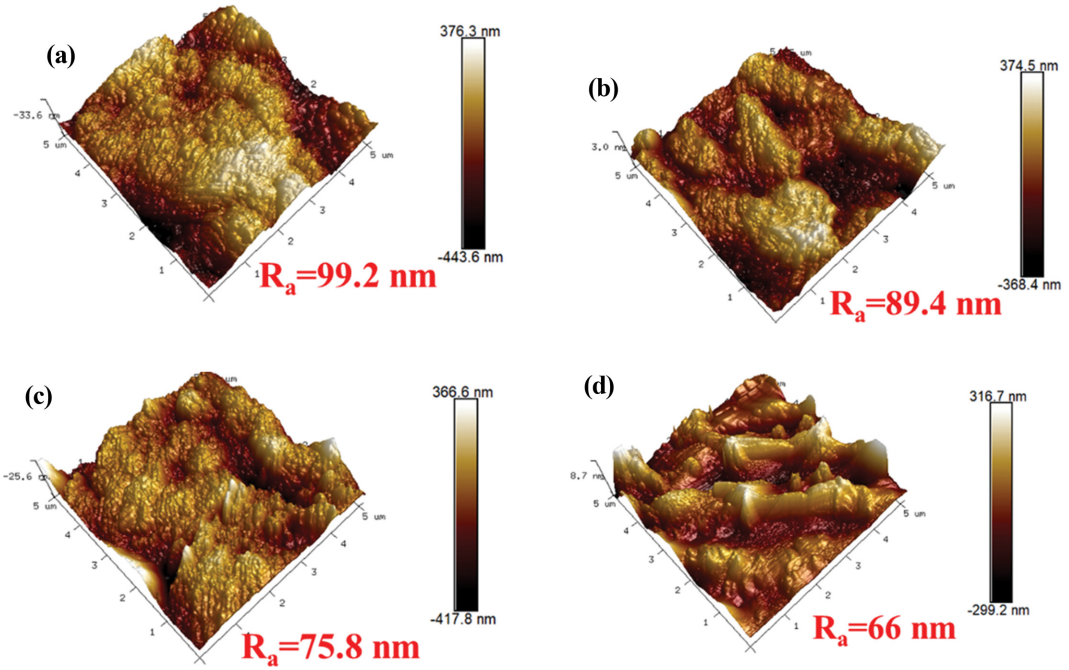

Fig. 10. AFM images of (a) M1, (b) M2, (c) M3, (d) M4.

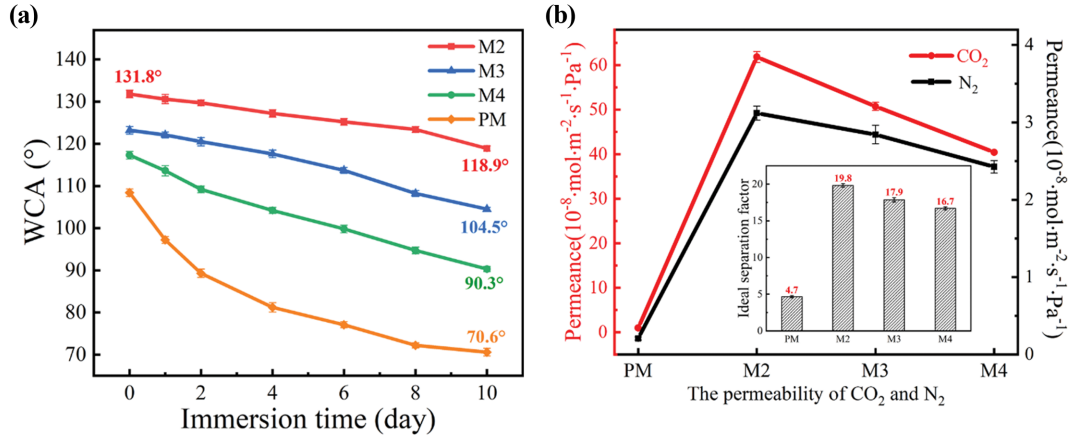

Fig. 11. The results of (a) the hydrophobic stability test and (b) the CO_2/N_2 permeability test.

tively low in comparison with other composite membranes, demonstrating that the filler particles do improve the gas permeability. This enhancement primarily results from the increase of microcavities introduced by filler particles [16,37]. The CO_2 permeance of the synthesized membranes is much bigger than that of N_2. In particular, the CO_2 permeance of M2 exceeds 60×10^{-8}·mol·m^{-2}·s^{-1}·Pa^{-1} with the CO_2/N_2 ideal selectivity of ~20. These decent outcomes could be mainly attributed to the fact that (1) CO_2 has a bigger diffusivity than N_2 in various membrane materials [38], (2) the pore structure and functional groups of filler ZIFs are beneficial for the permeance of CO_2 [22,39,40], and (3) the PDMS-MTES polymer is CO_2-philic [41,42]. Meanwhile, with the increase of the loading ratio of ZIF-L (accompanied by the decrease of ZIF-8), the permeability of both CO_2 and N_2 gradually decreases from M2 to M3 to M4. This phenomenon could be ascribed to the fact that when more nanoscale ZIF-8 particles are substituted by microscale ZIF-L, the microcavities within the dense coating will inevitably become more concentrated, which is harmful to the gas permeability. Whereas, the slight reduction of the CO_2/N_2 separation factor shows that the separation performance of these three membranes is very stable, which is a desirable characteristic.

6. CO_2 Absorption Performance in GLMC

Fig. 12(a) illustrates the CO_2 absorption performance of PM, M2, M3, M4. Overall, the CO_2 flux enhances with the rise of liquid velocity. But the enhancement is more noticeable when the velocity is at a lower level, which corresponds with the literature [43,44]. This phenomenon is because membrane pores are more likely to be wetted at a high liquid pressure [12,45]. The CO_2 absorption flux of M2, M3, M4 is much greater than that of PM, which matches well with the outcomes of the gas permeability test

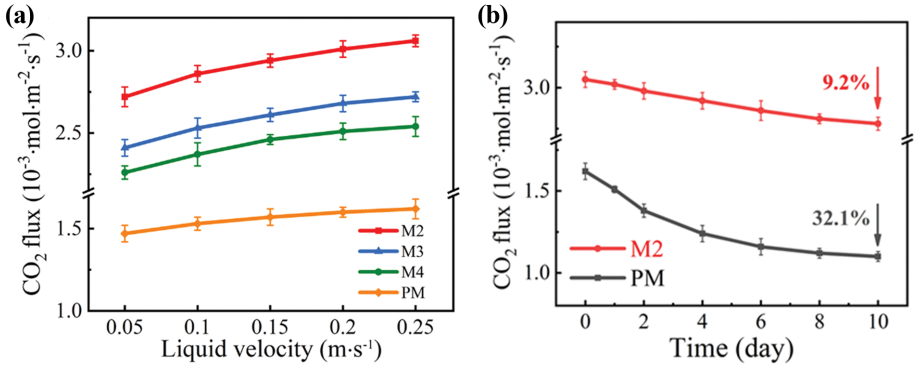

Fig. 12. (a) The CO_2 absorption flux and (b) long-term stability of the composite membrane.

Table 1. Comparison of the CO_2 absorption flux of different composite membranes

Membrane	Configuration	Feed gas	Absorption solvent	Liquid velocity	CO_2 absorption flux ($mmol \cdot m^{-2} \cdot s^{-1}$)	Ref.
PVDF/Graphene	Flat sheet	Pure CO_2	Water	0.012 $m \cdot s^{-1}$	3.0	[32]
PVDF/(fTiO$_2$-SiO$_2$)	Hollow fiber	Pure CO_2	Sodium taurinate solution	0.25 $m \cdot s^{-1}$	5.6	[46]
PVDF/mZIF-8	Hollow fiber	40% CO_2	Water	0.25 $m \cdot s^{-1}$	2.3	[19]
PVDF/mZIF-8	Hollow fiber	40% CO_2	1 M MEA	0.25 $m \cdot s^{-1}$	3.8	[19]
PVDF/silica	Flat sheet	50% CO_2	1 M AMP	100 $ml \cdot min^{-1}$	0.232	[16]
PEI/(silicon rubber)	Hollow fiber	Pure CO_2	Water	0.11 $m \cdot s^{-1}$	0.8	[47]
PVDF	Hollow fiber	Pure CO_2	Water	150 $ml \cdot min^{-1}$	0.6	[48]
PVDF/(ZIF-8-ZIF-L)	Flat sheet	Pure CO_2	1 M DEA	0.25 $m \cdot s^{-1}$	3.02	This work

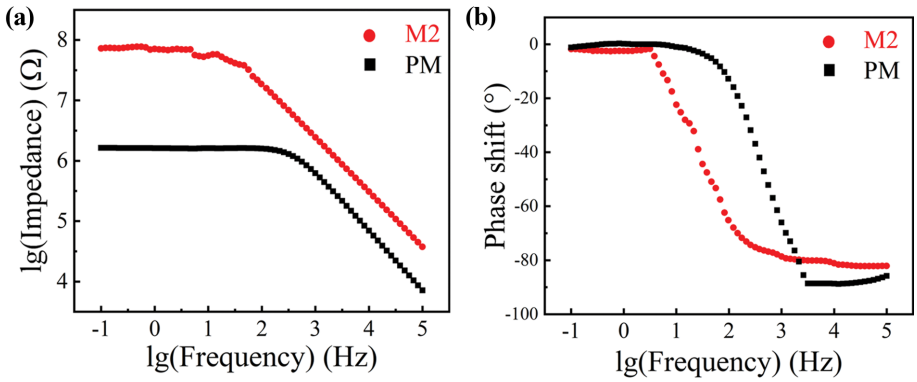

Fig. 13. Bode diagram of AC impedance test of M2 and PM.

and can be explained by the same mechanism. Meanwhile, the CO_2 absorption performance gradually deteriorates from M2 to M3 to M4. This may be ascribed to (1) the better hydrophobic stability of M2, implying that it is less likely to be wetted by absorbent in comparison with M3, M4, and (2) M2 possessing more uniformly distributed microcavities, which is beneficial for the absorption of CO_2. In particular, the CO_2 flux reaches $3.02 \times 10^{-3} \cdot mol \cdot m^{-2} \cdot s^{-1}$ when the liquid velocity is 0.25 $m \cdot s^{-1}$, which is comparable with the reported researches, as exhibited in Table 1.

A ten-day CO_2 absorption test was taken to examine the long-term operating stability of M2 and PM. In this experiment, gas and liquid rate are separately fixed at 1,000 $ml \cdot min^{-1}$ and 0.25 $m \cdot s^{-1}$. As shown in Fig. 12(b), the CO_2 flux of both M2 and PM continuously decreases with the progress of the experiment, indicating the occurrence of membrane wetting in this process. Through this test, the CO_2 flux decline of PM is 32.1%, while the number of M2 is only 9.2%, demonstrating its excellent hydrophobic stability.

7. Monitoring the Membrane Wetting Process

Fig. 13 shows the Bode diagram of PM and M2. When the phase shift in Fig. 13(b) is closely stable at 0° (the platform stage), the membrane impedance (the corresponding platform stage in Fig. 13(a)) represents the real membrane resistance [26]. Therefore, the test frequency of continuous impedance measurement is fixed at 1 Hz, which is located in the middle of the platform.

As shown in Fig. 14(a), the phase shift of both PM and M2 is closely stable at 0°, indicating the successful implementation of con-

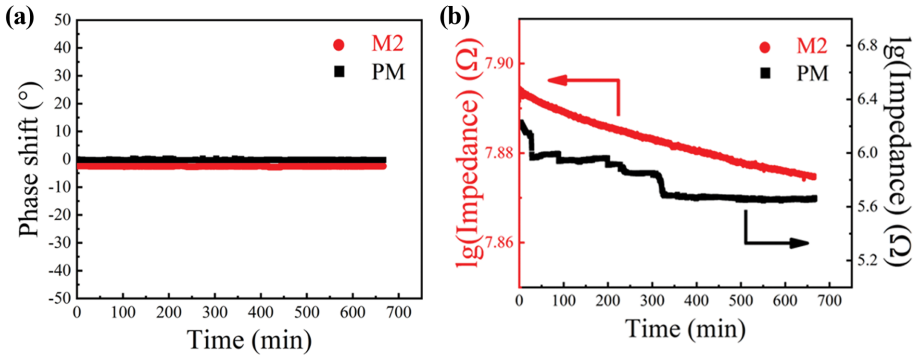

Fig. 14. Continuous impedance test of M2 and PM in 1 mol/L DEA solution.

tinuous impedance test. In Fig. 14(b), the impedance of M2 is much greater than that of PM throughout the whole experiment, implying the addition of ZIFs filler particles increases the membrane resistance. The falling impedance of PM and M2 indicates the occurrence of membrane wetting, which seems inevitable in the long-time contact with 1 mol/L DEA solution. But the declining trend of M2 is much smoother than that of PM, which undergoes several sharp drops; this may be attributed to the better hydrophobic stability of M2. Also noteworthy is that the impedance decline of M2 is only 0.21% in this nearly 12-hour test, indicating its excellent anti-wetting ability. Meanwhile, this accounts for why there is only a slight drop in performance at the initial stage of both the hydrophobic stability test and the long-term CO_2 absorption process.

CONCLUSIONS

ZIF-8 nanocrystals and ZIF-L nanosheets were simultaneously incorporated into PDMS-MTES polymer to synthesize the hydrophobic composite membrane with high CO_2 absorption performance. The effect of ZIFs particles on the composite membrane properties was thoroughly investigated. Also, the optimum loading ratio of ZIFs/PDMS was achieved after a series of characterizations and experiments. And when 30 wt% ZIF-8 nanoparticles and 10 wt% ZIF-L nanosheets were uniformly incorporated, we obtained the desirable composite membrane. It displayed both excellent hydrophobic stability and CO_2 permeability. More importantly, this membrane exhibited competitive CO_2 absorption flux and long-term operating stability. And it also possessed excellent anti-wetting ability in the continuous impedance test. Consequently, this work offers a new synthesis method to fabricate high-performance hydrophobic composite membranes for CO_2 absorption in membrane contactor.

ACKNOWLEDGEMENT

Financial support from the National Natural Science Foundation of China (21576011) is gratefully acknowledged.

REFERENCES

1. C. A. Scholes, S. E. Kentish, G. W. Stevens, J. Jin and D. deMontigny, *Sep. Purif. Technol.*, **156**, 841 (2015).
2. Z. Qi and E. L. Cussler, *J. Membr. Sci.*, **23**, 321 (1985).
3. S. Nii, H. Takeuchi and K. Takahashi, *J. Chem. Eng. Jpn.*, **25**, 67 (1992).
4. S. Karoor and K. K. Sirkar, *Ind. Eng. Chem. Res.*, **32**, 674 (1993).
5. S. Nii and H. Takeuchi, *Gas Sep. Purif.*, **8**, 107 (1994).
6. D. deMontigny, P. Tontiwachwuthikul and A. Chakma, *J. Membr. Sci.*, **277**, 99 (2006).
7. S. M. Sedghi, J. Brisson, D. Rodrigue and M. C. Iliuta, *Sep. Purif. Technol.*, **80**, 338 (2011).
8. P. Keshavarz, J. Fathikalajahi and S. Ayatollahi, *J. Hazard. Mater.*, **152**, 1237 (2008).
9. S. Khaisri, D. deMontigny, P. Tontiwachwuthikul and R. Jiraratananon, *Sep. Purif. Technol.*, **65**, 290 (2009).
10. S. Rajabzadeh, S. Yoshimoto, M. Teramoto, M. Al-Marzouqi and H. Matsuyama, *Sep. Purif. Technol.*, **69**, 210 (2009).
11. H.-Y. Zhang, R. Wang, D. T. Liang and J. H. Tay, *J. Membr. Sci.*, **308**, 162 (2008).
12. S. Mosadegh-Sedghi, D. Rodrigue, J. Brisson and M. C. Iliuta, *J. Membr. Sci.*, **452**, 332 (2014).
13. Z. Dai, L. Ansaloni and L. Deng, *Ind. Eng. Chem. Res.*, **55**, 5983 (2016).
14. C. A. Scholes, S. E. Kentish, G. W. Stevens and D. deMontigny, *Int. J. Greenh. Gas Control.*, **42**, 66 (2015).
15. K. Li, X. Zeng, H. Li, X. Lai, C. Ye and H. Xie, *Appl. Surf. Sci.*, **279**, 458 (2013).
16. A. Rosli, A. L. Ahmad and S. C. Low, *Sep. Purif. Technol.*, **221**, 275 (2019).
17. J. Yao and H. Wang, *Chem. Soc. Rev.*, **43**, 4470 (2014).
18. Q. Song, S. K. Nataraj, M. V. Roussenova, J. C. Tan, D. J. Hughes, W. Li, P. Bourgoin, M. A. Alam, A. K. Cheetham, S. A. Al-Muhtaseb and E. Sivaniah, *Energy Environ. Sci.*, **5**, 8359 (2012).
19. Y. Xu, X. Li, Y. Lin, C. Malde and R. Wang, *J. Membr. Sci.*, **585**, 238 (2019).
20. H. Fan, Q. Shi, H. Yan, S. Ji, J. Dong and G. Zhang, *Angew. Chem. Int. Ed.*, **53**, 5578 (2014).
21. W.-C. Lee, L. Bondaz, S. Huang, G. He, M. Dakhchoune and K. V. Agrawal, *J. Membr. Sci.*, **618**, 118745 (2021).
22. R. Chen, J. Yao, Q. Gu, S. Smeets, C. Baerlocher, H. Gu, D. Zhu, W. Morris, O. M. Yaghi and H. Wang, *Chem. Commun.*, **49**, 9500 (2013).
23. H. Mao, H.-G. Zhen, A. Ahmad, S.-H. Li, Y. Liang, J.-F. Ding, Y. Wu, L.-Z. Li and Z.-P. Zhao, *J. Membr. Sci.*, **582**, 307 (2019).

24. H. Li, L. Han, J. Hou, J. Liu and Y. Zhang, *J. Membr. Sci.*, **572**, 82 (2019).
25. S. Bannwarth, M. Darestani, H. Coster and M. Wessling, *J. Membr. Sci.*, **473**, 318 (2015).
26. J. Xiao, Q. Sun, L. Liu and Z. Ding, *Chin. J. Chem. Eng.*, In press (2020).
27. J. Cravillon, S. Münzer, S.-J. Lohmeier, A. Feldhoff, K. Huber and M. Wiebcke, *Chem. Mater.*, **21**, 1410 (2009).
28. Q. Huang, Q. Luo, Z. Chen, L. Yao, P. Fu and Z. Lin, *Environ. Sci.: Water Res. Technol.*, **4**, 1145 (2018).
29. I. U. Khan, M. H. D. Othman, A. F. Ismail, N. Ismail, J. Jaafar, H. Hashim, M. A. Rahman and A. Jilani, *Mater. Charact.*, **136**, 407 (2018).
30. Z.-X. Low, J. Yao, Q. Liu, M. He, Z. Wang, A. K. Suresh, J. Bellare and H. Wang, *Cryst. Growth Des.*, **14**, 6589 (2014).
31. G. Liu, Z. Jiang, K. Cao, S. Nair, X. Cheng, J. Zhao, H. Gomaa, H. Wu and F. Pan, *J. Membr. Sci.*, **523**, 185 (2017).
32. X. Wu, B. Zhao, L. Wang, Z. Zhang, H. Zhang, X. Zhao and X. Guo, *J. Membr. Sci.*, **520**, 120 (2016).
33. Y. Pan, Y. Hang, X. Zhao, G. Liu and W. Jin, *J. Membr. Sci.*, **579**, 210 (2019).
34. H. Li, Y.-M. Chen, X.-T. Ma, J.-L. Shi, B.-K. Zhu and L.-P. Zhu, *J. Membr. Sci.*, **379**, 397 (2011).
35. M. Rezakazemi, A. Vatani and T. Mohammadi, *RSC Adv.*, **5**, 82460 (2015).
36. Z.-X. Low, A. Razmjou, K. Wang, S. Gray, M. Duke and H. Wang, *J. Membr. Sci.*, **460**, 9 (2014).
37. V. Vatanpour, S. S. Madaeni, A. R. Khataee, E. Salehi, S. Zinadini and H. A. Monfared, *Desalination*, **292**, 19 (2012).
38. X. Zhang, X. He and T. Gundersen, *Energy Fuels*, **27**, 4137 (2013).
39. R. Banerjee, H. Furukawa, D. Britt, C. Knobler, M. O'Keeffe and O. M. Yaghi, *J. Am. Chem. Soc.*, **131**, 3875 (2009).
40. Y. Hu, Z. Liu, J. Xu, Y. Huang and Y. Song, *J. Am. Chem. Soc.*, **135**, 9287 (2013).
41. W. Qiang, D. Hu, T. Liu and L. Zhao, *J. Supercrit. Fluids*, **147**, 329 (2019).
42. M. K. Barillas, R. M. Enick, M. O'Brien, R. Perry, D. R Luebke and B. D. Morreale, *J. Membr. Sci.*, **372**, 29 (2011).
43. Y. Lin, Y. Xu, C. H. Loh and R. Wang, *Appl. Surf. Sci.*, **436**, 670 (2018).
44. H.-Y. Zhang, R. Wang, D. T. Liang and J. H. Tay, *J. Membr. Sci.*, **279**, 301 (2006).
45. J.-L. Li and B.-H. Chen, *Sep. Purif. Technol.*, **41**, 109 (2005).
46. Y. Xu, Y. Lin, M. Lee, C. Malde and R. Wang, *J. Membr. Sci.*, **552**, 253 (2018).
47. S. A. Hashemifard, A. F. Ismail, T. Matsuura and M. R. DashtArzhandi, *RSC Adv.*, **5**, 48442 (2015).
48. A. Mansourizadeh and S. Mousavian, *J. Polym. Res.*, **20**, 99 (2013).